

Four New Mn^{II} Inorganic–Organic Hybrid Frameworks with Diverse Inorganic Magnetic Chain's Sequences: Syntheses, Structures, Magnetic, NLO, and Dielectric Properties

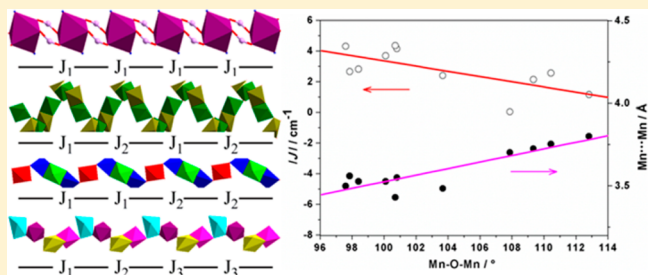
Chong-Bin Tian,[†] Chao He,[†] Yun-Hu Han,^{†,‡} Qi Wei,^{†,‡} Qi-Peng Li,^{†,‡} Ping Lin,[†] and Shao-Wu Du^{*,†}

[†]State Key Laboratory of Structural Chemistry, Fujian Institute of Research on the Structure of Matter, Chinese Academy of Sciences, Fuzhou, Fujian 350002, P. R. China

[‡]Graduate University of Chinese Academy of Sciences, Beijing 100039, P. R. China

S Supporting Information

ABSTRACT: Four new inorganic–organic hybrid manganese frameworks, formulated as $[\text{Mn}(\text{Am-Hip})_2] \cdot 3\text{H}_2\text{O}$ (**1**), $[\text{Mn}_2(\text{ip})_2(\text{H}_2\text{O})] \cdot \text{CH}_3\text{OH}$ (**2**), $[\text{Mn}_2(\text{OH-ip})_2(\text{DMF})] \cdot \text{DMF}$ (**3**), and $(\text{Me}_2\text{NH}_2)[\text{Mn}_4(\text{sdba})_4(\text{Hsdba})(\text{H}_2\text{O})] \cdot 3\text{H}_2\text{O} \cdot 2\text{DMF}$ (**4**) (Am-Hip = 5-aminoisophthalic acid, H_2ip = isophthalic acid, OH-Hip = 5-hydroxyisophthalic acid, and H_2sdba = 4,4'-sulfonyldibenzonic acid), have been prepared by solvothermal reactions of Mn^{II} ions with different polycarboxylate acids in the presence of LiNO_3 or NH_4NO_3 . Single-crystal X-ray diffraction studies reveal that the frameworks of **1–4** contain diverse Mn^{II}–oxygen inorganic magnetic chain's sequences, $-\text{J}_1\text{J}_1\text{J}_1-$ for **1**, $-\text{J}_1\text{J}_2\text{J}_1-$ for **2**, $-\text{J}_1\text{J}_2\text{J}_2-$ for **3**, and $-\text{J}_1\text{J}_2\text{J}_3-$ for **4**. The sequence in **4** has never been seen for the magnetic chain compounds and is a new type of magnetic alternating sequence. Magnetic investigations indicate that these compounds all show weak antiferromagnetic couplings between the adjacent Mn^{II} ions. Magnetostructural analyses based on the data of **1–4** and other related Mn^{II} chain compounds imply that the magnitude of the magnetic coupling has some relationship with the Mn–O–Mn angle of the μ_2 -O bridge and the average Mn–O–C–O torsion angle of the carboxylate bridges. Compounds **2** and **4** crystallize in chiral and acentric space groups, and they both exhibit powder second harmonic generation (SHG) efficiencies approximately 0.6 and 0.9 times, respectively, that of the standard potassium dihydrogen phosphate (KDP) powder. In addition, the dielectric properties of **2** and **4** were also investigated.



INTRODUCTION

Inorganic–organic hybrid materials are very attractive because they combine dissimilar components in one material, which can provide the opportunity to invent an almost unlimited set of new materials with multifunctional properties.¹ In particular, 1D ordered inorganic magnetic chains and their extended inorganic–organic hybrid solids with paramagnetic metal centers have received growing attention due to the recent discovery of single-chain magnets² and because some of them can serve as excellent models for the theoretical calculation aiming at a better understanding of the magneto-structure correlation.³ Owing to the diversiform bridging modes of azide, so far, the strategy to construct inorganic–organic hybrid frameworks with inorganic magnetic chains has been mainly focused on using azide as a bridging ligand.⁴ As a result, a considerable number of inorganic–organic hybrid Mn^{II} frameworks with alternating inorganic Mn^{II}–nitrogen chain's sequences have been obtained during the last decades, such as $-\text{J}_1\text{J}_2-$,⁵ $-\text{J}_1\text{J}_1\text{J}_2-$,⁶ $-\text{J}_1\text{J}_1\text{J}_2\text{J}_2-$,⁷ $-\text{J}_1\text{J}_2\text{J}_3\text{J}_2-$,⁸ and $-\text{J}_1\text{J}_2\text{J}_3\text{J}_3-$.⁹ In comparison, those with inorganic Mn(II)–oxygen magnetic chain's sequences are still fairly rare.¹⁰ It is not surprising since the construction of such compounds not only

requires the metal oxygen polyhedron to share corners or edges with the adjacent one along one direction but also needs different bridging modes of carboxylate groups among the paramagnetic centers.

Carboxylic ligands are good candidates for building hybrid compounds because of their versatile coordination modes with metal ions. Meanwhile, the Mn^{II} ion is well-recognized from the magnetic point of view as it contains high-spin d⁵ configuration and nearly no spin orbital contribution to magnetic moment. Thus, the assembly of Mn^{II} with various carboxylic acids results in some Mn^{II}–carboxylate compounds, ranging from discrete clusters to multidimensional hybrid frameworks.^{10,11} In the compounds with 1D Mn^{II}–carboxylate chains, the neighboring Mn^{II} ions can be bridged not only by a single $\mu_{1,3}$ -carboxylate (*syn-syn*, *syn-anti*, or *anti-anti*), but also by two or three carboxylates with a mixed $\mu_{1,3}$ -carboxylate/ μ_2 -O coordination mode. Magneto-structural correlation investigation indicates that the *syn-syn* carboxylate group normally gives rise to an antiferromagnetic exchange pathway between the metal centers,

Received: November 4, 2014

Published: February 27, 2015

and the magnetic interaction through this pathway is larger than that for the *syn-anti* or *anti-anti* carboxylates.¹² For the mixed carboxylato bridges, various attempts have been made to account for the magnetic coupling nature and magnitude in the light of structural parameters such as bond lengths, bond angles, and bridging types of the ligands.^{10c,e,13} However, a systematic magneto-structural correlation has not been established for such system, though it is of utmost importance to understanding the magnetic mechanism of molecule-based magnetic material.

On the other hand, second-order nonlinear optical (NLO) and dielectric materials have received increasing attention due to their potential applications as functional materials.¹⁴ Traditionally, investigations of second-order NLO and dielectric materials were mainly focused on inorganic compounds, such as potassium dihydrogen phosphate (KDP), lithium niobate (LiNbO_3), barium titanate (BaTiO_3), and zirconium oxide (ZrO_2).¹⁵ Inorganic–organic hybrid frameworks, which combine the high NLO coefficients of the organic molecules with excellent physical properties of the inorganics, appear to be promising candidates for NLO and dielectric materials. So far as we know, several inorganic–organic hybrid materials have been reported to exhibit second-order NLO property.¹⁶ However, the assembly of inorganic–organic hybrid materials with both second-order NLO and dielectric properties is still a big challenge because such compounds not only need to crystallize in the noncentrosymmetric space groups but also must contain polarization molecules, dipolar reorientation, or ion displacement.¹⁷

Herein, we report the synthesis and characterization of four new inorganic–organic hybrid Mn^{II} frameworks, $[\text{Mn}(\text{Am-Hip})_2] \cdot 3\text{H}_2\text{O}$ (**1**), $[\text{Mn}_2(\text{ip})_2(\text{H}_2\text{O})] \cdot \text{CH}_3\text{OH}$ (**2**), $[\text{Mn}_2(\text{OH-ip})_2(\text{DMF})] \cdot \text{DMF}$ (**3**), and $(\text{Me}_2\text{NH}_2)[\text{Mn}_4(\text{sdba})_4(\text{Hsdba})(\text{H}_2\text{O})] \cdot 3\text{H}_2\text{O} \cdot 2\text{DMF}$ (**4**) ($\text{Am-H}_2\text{ip}$ = 5-aminoisophthalic acid, H_2ip = isophthalic acid, $\text{OH-H}_2\text{ip}$ = 5-hydroxyisophthalic acid, and H_2sdba = 4, 4'-sulfonyldibenzoinoic acid). Single-crystal X-ray diffraction studies reveal that **1** is a 2D coordination polymer based on infinite $\text{Mn}-\text{O}-\text{C}-\text{O}$ uniform chains, while **2–4** are all 3D frameworks constructed by infinite inorganic Mn^{II} –oxygen chains with different alternating inorganic magnetic chain's sequences. Compound **2** shows a helical alternating inorganic $-\text{J}_1\text{J}_2-$ magnetic sequence, **3** exhibits a rare periodic inorganic $-\text{J}_1\text{J}_1\text{J}_2\text{J}_2-$ magnetic sequence, and **4** displays a novel $-\text{J}_1\text{J}_3\text{J}_3-$ magnetic sequence. Magnetic property measurements indicate that **1–4** display antiferromagnetic coupling between adjacent Mn^{II} ions. Comparison of these compounds with previously reported analogues provides useful information on magneto-structure correlations. In addition, the NLO and dielectric properties of **2** and **4** were also investigated.

EXPERIMENTAL SECTION

Materials and Physical Measurements. All the chemicals were purchased from commercial sources and used without further purification. Thermogravimetric experiments were performed using a GA/NETZSCH STA449C instrument heated from 30 to 800 °C (heating rate of 10 °C min⁻¹, nitrogen stream). DSC (differential scanning calorimetry) measurements were performed on the NETZSCH DTA404PC with heating rate of 5 K/min under nitrogen atmosphere. Elemental analyses of C, H, and N were carried out with a Vario EL III elemental analyzer. High-resolution PXRD patterns were collected using PANalytical X'Pert Pro diffractometer ($\text{Cu K}\alpha$ radiation: $\lambda = 1.54056 \text{ \AA}$) in the range $5^\circ < 2\theta < 60^\circ$. IR spectra were performed on a PerkinElmer Spectrum One spectrometer using KBr as pellets over the range 4000–400 cm⁻¹. Magnetic properties

were measured on polycrystalline samples with a Quantum Design PPMS-9T system. The susceptibility data was collected under an applied magnetic field of 1 kOe in the temperature range 2–300 K. Diamagnetic corrections were made using Pascal's constants. The EPR measurements were performed with a Bruker ELEXSYS E500 spectrometer at room temperature. The NLO properties of **2** and **4** were tested on microcrystalline samples with a particle size around 100 μm by the Kurtz and Perry method using an Nd:YAG laser (1064 nm) with input pulse of 350 mV. KDP powder with similar particle size was also measured to serve as a reference. The solid-state CD experiments were performed on a MOS-450 spectropolarimeter at room temperature using a mixture of **2** and dried KCl powder, which were well-grounded and then pressed into a disk before use. The temperature-dependent ac dielectric constant measurements for **2** and **4** were carried out with a Solartron 1260 impedance analyzer. The ferroelectric hysteresis loops for **2** and **4** were recorded on an aix-ACCT TF2000 analyzer at room temperature using a powder sample in pellet.

Synthesis of $[\text{Mn}(\text{Am-Hip})_2] \cdot 3\text{H}_2\text{O}$ (1**).** A mixture of $\text{Mn}(\text{ClO}_4)_2 \cdot 6\text{H}_2\text{O}$ (0.25 mmol, 0.09 g), $\text{Am-H}_2\text{ip}$ (0.50 mmol, 0.09 g), and NH_4NO_3 (0.50 mmol, 0.04 g) was placed in 20 mL of Teflon-lined stainless steel vessel with a mixed-solvent of CH_3CN (4 mL) and CH_3OH (3 mL), and was heated at 160 °C for 2 days under autogenous pressure. After cooling to room temperature, colorless prismatic crystals of **1** were obtained. Yield: 0.073 g (64% based on Mn). Anal. Calcd for $\text{C}_{18}\text{H}_{15}\text{MnN}_3\text{O}_8$ (456.27): C 47.38, H 3.31, N 9.21. Found: C 47.09, H 3.28, N 9.16. IR (KBr, cm⁻¹): 3434 w, 3313 w, 3134 m, 1682 vw, 1608 w, 1551 m, 1400 s, 1375 s, 1314 vw, 1256 vw, 1160 vw, 1018 vw, 995 vw, 958 w, 895 vw, 767 w, 703 w, 592 vw.

Synthesis of $[\text{Mn}_2(\text{ip})_2(\text{H}_2\text{O})] \cdot \text{CH}_3\text{OH}$ (2**).** The procedure was similar to that described for **1** except H_2ip was used instead of $\text{Am-H}_2\text{ip}$. Colorless prismatic crystals of **2** were obtained. Yield: 0.042 g (69% based on Mn). Anal. Calcd for $\text{C}_{17}\text{H}_{14}\text{Mn}_2\text{O}_{10}$ (488.16): C 41.83, H 2.89. Found: C 41.55, H 2.82. IR (KBr, cm⁻¹): 3434 m, 1609 s, 1552 s, 1475 m, 1446 m, 1388 s, 1319 vw, 1273 vw, 1168 w, 1089 vw, 1005 vw, 944 vw, 918 vw, 837 vw, 807 vw, 750 m, 721 vw, 711 m, 657 w, 570 vw.

Synthesis of $[\text{Mn}_2(\text{OH-ip})_2(\text{DMF})] \cdot \text{DMF}$ (3**).** A mixture of $\text{Mn}(\text{CH}_3\text{COO})_2 \cdot 4\text{H}_2\text{O}$ (0.25 mmol, 0.061 g), $\text{OH-H}_2\text{ip}$ (0.50 mmol, 0.09 g), and LiNO_3 (0.50 mmol, 0.035 g) was placed in a 20 mL of Teflon-lined stainless steel vessel with 5 mL of DMF (*N,N'*-dimethylformamide), and was heated at 160 °C for 2 days under autogenous pressure. After cooling to room temperature, colorless flaky crystals of **3** were obtained. Yield: 0.061 g (79% based on Mn). Anal. Calcd for $\text{C}_{22}\text{H}_{22}\text{Mn}_2\text{N}_2\text{O}_{12}$ (616.30): C 42.88, H 3.59, N 4.54. Found: C 42.42, H 3.51, N 4.45. (KBr, cm⁻¹): 3363 m, 3132 m, 1662 w, 1640 s, 1559 s, 1488 m, 1399 s, 1282 m, 1228 m, 1099 m, 1002 w, 975 w, 927 vw, 909 w, 883 vw, 807 w, 782 m, 726 w, 716 w, 666 w, 584 w, 468 vw.

Synthesis of $(\text{Me}_2\text{NH}_2)[\text{Mn}_4(\text{sdba})_4(\text{Hsdba})(\text{H}_2\text{O})] \cdot 3\text{H}_2\text{O} \cdot 2\text{DMF}$ (4**).** A mixture of $\text{Mn}(\text{ClO}_4)_2 \cdot 6\text{H}_2\text{O}$ (0.50 mmol, 0.18 g), H_2sdba (1.0 mmol, 0.31 g), and NH_4NO_3 (0.50 mmol, 0.04 g) was placed in a 20 mL of Teflon-lined stainless steel vessel with 10 mL of DMF, and was heated at 160 °C for 2 days under autogenous pressure. After cooling to room temperature, colorless prismatic crystals of **4** were obtained. Yield: 0.185 g (74% based on Mn). Anal. Calcd for $\text{C}_{78}\text{H}_{71}\text{Mn}_4\text{N}_3\text{O}_{36}\text{S}_5$ (2006.47): C 46.69, H 3.57, N 2.09. Found: C 46.33, H 3.51, N 2.02. IR (KBr, cm⁻¹): 3434 m, 3099 vw, 3071 vw, 3039 vw, 2967 vw, 2929 vw, 2797 vw, 1712 vw, 1654 m, 1616 vw, 1597 s, 1553 s, 1490 m, 1465 vw, 1407 vs, 1324 m, 1298 s, 1163 s, 1137 m, 1101 m, 1070 w, 1014 w, 870 w, 782 w, 740 s, 720 w, 697 w, 620 s, 578 m, 490 vw, 469 w.

Single-Crystal Structure Determination. Single crystals of compounds **1–4** suitable for X-ray diffraction were carefully selected and glued to thin glass fibers with epoxy resin. Intensity data were collected at room temperature on a Rigaku Mercury CCD area-detector diffractometer with a graphite monochromator utilizing $\text{Mo K}\alpha$ radiation ($\lambda = 0.71073 \text{ \AA}$). *Crystalclear* software¹⁸ was used for data reduction and empirical absorption correction. The structures were solved by direct methods and refined on F^2 by full-matrix least-

Table 1. Crystallographic Data for Complexes 1–4

	1	2M	2P	3	4
empirical formula	C ₁₆ H ₁₈ MnN ₂ O ₁₁	C ₁₇ H ₁₄ Mn ₂ O ₁₀	C ₁₇ H ₁₄ Mn ₂ O ₁₀	C ₂₂ H ₂₂ Mn ₂ N ₂ O ₁₂	C ₇₂ H ₄₇ Mn ₄ NO ₃₁ S ₅
fw	469.26	488.16	488.16	616.30	1351.95
cryst syst	monoclinic	tetragonal	tetragonal	triclinic	monoclinic
space group	C2/c	P4 ₃	P4 ₁	P $\bar{1}$	Cc
a/Å	28.045(19)	13.0721(4)	13.0696(3)	9.745(3)	23.604(8)
b/Å	4.536(3)	13.0721(4)	13.0696(3)	11.845(4)	41.954(12)
c/Å	15.579(11)	11.1466(5)	11.2867(5)	12.554(3)	11.675(4)
α/deg	90.00	90.00	90.00	62.439(13)	90.00
β/deg	116.200(7)	90.00	90.00	71.799(17)	116.908(4)
γ/deg	90.00	90.00	90.00	75.241(17)	90.00
V/Å ³	1780(2)	1904.73(12)	1927.93(11)	1209.9(6)	10 310(6)
Z	4	4	4	2	4
D _{calc} /g cm ⁻³	1.751	1.702	1.682	1.709	1.161
μ/mm^{-1}	0.812	1.380	1.363	1.125	0.645
F(000)	964	984	984	628	1410
params	144	252	262	374	1006
R1 ^a , wR2 ^b [I > 2σ(I)]	0.0550/0.1557	0.0735/0.1916	0.0455/0.1278	0.0462/0.1242	0.0612/0.1635
R1 ^a , wR2 ^b [all data]	0.0600/0.1610	0.0994/0.2212	0.0488/0.1301	0.0663/0.1347	0.0840/0.1873
GOF	1.012	1.034	1.012	1.010	1.038
Flack param		0.02(5)	0.02(2)		0.101(18)

^aR1 = $\sum |F_o| - |F_c| / \sum |F_o|$. ^bwR2 = [$\sum w(F_o^2 - F_c^2)^2 / \sum w(F_o^2)^2$]^{0.5}.

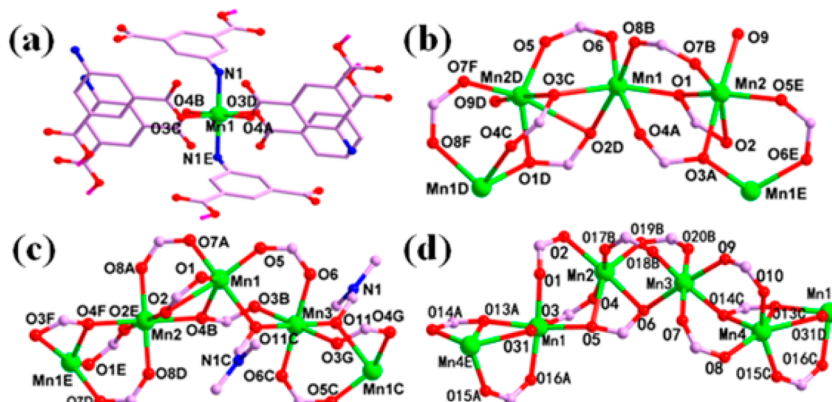


Figure 1. Coordination environment of Mn^{II} ions in 1 (a), 2 (b), 3 (c), and 4 (d). Hydrogen atoms and lattice solvent molecules are omitted for clarity.

squares using the SHELXL-97 program package.¹⁹ All non-hydrogen atoms were refined anisotropically. The hydrogen atoms bonded to carbon were generated geometrically (C–H 0.97 or 0.93 Å) and U(H) values set as 1.2 times Ueq(C). Attempts to locate and model the highly disordered solvent molecules in the pores were unsuccessful. Therefore, the PLATON/SQUEEZE²⁰ was used to compensate the data for their contribution to the diffraction patterns for 4. The final chemical formula of 4 was calculated from SQUEEZE results combined with the TGA and elemental analysis data. The crystallographic data for 1–4 are listed in Table 1. Selected bond lengths (Å) and angles (deg) for these compounds are listed in Tables S1–S4 (Supporting Information). CCDC numbers for 1–4 are 1031797–1031801.

RESULTS AND DISCUSSION

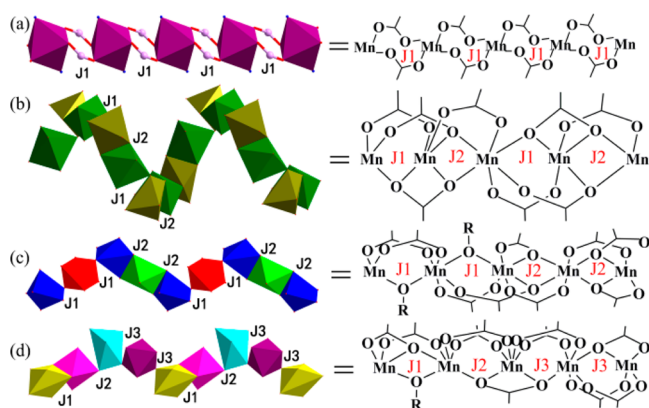
Syntheses and IR Spectral Analysis. Solvothermal synthesis has been proven to be a convenient and powerful synthetic technique for the preparation of inorganic–organic hybrid frameworks. Compounds 1–4 were obtained by the reactions of Mn^{II} salts with R-isophthalic acids (R = –Am, –H, –OH) or 4,4'-sulfonyldibenzoic acid and NH₄NO₃ or LiNO₃ with the molar ratio of 1:2:2 under solvothermal conditions.

Compounds 1 and 2 were formed in a mixed solvent of acetonitrile and methanol in the presence of NH₄NO₃, while 3 and 4 were produced in a pure solvent of DMF in the existence of LiNO₃. Here, NH₄NO₃ and LiNO₃ serve as templates for the absence of them yields no products from this system. The elemental analyses for 1–4 were in good agreement with the theoretical values. Powder X-ray diffraction (PXRD) has been used to check the phase purity of bulk samples in the solid state. The measured PXRD patterns of 1–4 are well-matched with the simulated patterns generated from the results of single-crystal X-ray diffraction data (Supporting Information, Figure S1), indicating phase purity of the as-synthesized samples. For 1–4, the characteristic bands of the carboxyl groups are observed in the ranges 1551–1640 and 1375–1490 cm⁻¹, corresponding to the asymmetric and symmetric stretching modes, respectively. The presence of an absorption peak at around 1700 cm⁻¹ in the IR spectra of 1 and 4 suggests that the carboxyl groups in these two compounds are not completely deprotonated (Supporting Information, Figure S2a,d).

Crystal Structure of [Mn(Am-Hip)₂]·3H₂O (1). Single-crystal X-ray diffraction study shows that 1 crystallizes in the

space group $C2/c$ and is a three-dimensional supramolecular architecture constructed by infinite $Mn-O-C-O$ chains. Its asymmetric unit contains half Mn^{II} ion, one $Am\text{-}Hip}^-$ anion, and one and a half lattice H_2O molecules (Supporting Information, Figure S3a). The Mn1 atom has an elongated distorted octahedral coordination geometry and is ligated by four carboxylate oxygen atoms in the equatorial position ($Mn-O = 2.170\text{--}2.176 \text{ \AA}$) and two nitrogen atoms in the axial position ($Mn1-N1 = 2.321 \text{ \AA}$) (Figure 1a). The neighboring Mn^{II} ions are connected into a 1D infinite $Mn-O-C-O$ chain through double *syn-anti* carboxylate bridges (Scheme 1a)

Scheme 1. Schematic Representation of the Diverse Inorganic Magnetic Chain's Sequences, (a) for 1, (b) for 2, (c) for 3, and (d) for 4, Showing the J Pathways



along the b axis, with a $Mn\cdots Mn$ distance of 4.54 \AA , which is comparable to other closely related compounds ($4.50\text{--}4.79 \text{ \AA}$).^{13c,21} According to a simple scheme suggested by Cheetham and co-workers, inorganic–organic hybrid frameworks can be symbolized as I^mO^n , where m and n represent the dimensionality of inorganic (I) and organic (O) connectivities, respectively.^{1a} Therefore, the 1D $Mn-O-C-O$ chain in **1** can be viewed as I^0O^1 hybrid (Figure 2a). These 1D chains are

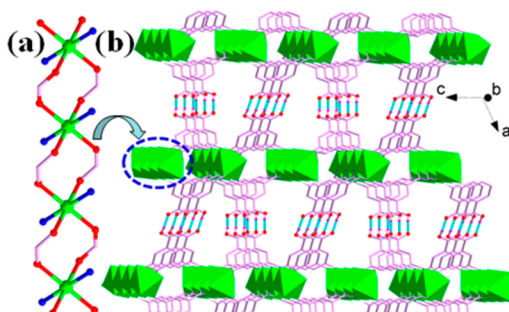


Figure 2. (a) View of the 1D chain in **1**. (b) View of 3D supramolecular architecture of **1** constructed by hydrogen bonding.

linked into a 2D sheet (I^0O^2 type) through Am-Hip⁻ ligands that adopt a $k^1\text{-}(k^1-k^1)\text{-}\mu_3$ bridging mode. The 2D layers are extended by hydrogen bonding interactions ($O\cdots O = 2.61 \text{ \AA}$, $H\cdots O = 1.80 \text{ \AA}$, $O-H\cdots O = 174.44^\circ$) to generate a 3D supramolecular architecture (Figure 2b). In the structure of **1**, the Am-Hip⁻ ligand can be viewed as a 3-connecting node, while the Mn1 center can be regarded as a 6-connecting node. Thus, compound **1** can be abstracted into a 2D (3,6)-connected **kgd** net (Supporting Information, Figure S3b).

Crystal Structure of $[Mn_2(ip)_2(H_2O)]\cdot CH_3OH$ (2). Single-crystal X-ray diffraction study reveals that the spontaneous resolution occurs during the crystallization of **2**, resulting in a pair of enantiomers **2P** and **2M**, which crystallize in chiral space groups $P4_1$ and $P4_3$ with Flack parameters being $0.02(5)$ and $0.02(2)$, respectively. Herein, only the structure of **2P** was described in detail. The asymmetric unit of **2P** consists of two Mn^{II} ions, two ip^{2-} anions, one coordinated H_2O molecule, and one free MeOH molecule (Supporting Information, Figure S4). Both the Mn1 and Mn2 atoms are six-coordinate, adopting a distorted MnO_6 octahedral geometry with different coordination environments: Mn1 atom is surrounded by six carboxylate oxygen atoms from six different ip^{2-} anions, while Mn2 is coordinated by five carboxylate oxygen atoms and one oxygen atom from the coordinated water molecule (Figure 1b). Each $Mn1O_6$ octahedron shares a corner (O1) and an edge (O2D...O3C) with the two neighboring $Mn2O_6$ octahedra, respectively, forming an infinite $Mn-O-Mn$ inorganic helical connectivity (I^1O^0) with a pitch of 11.287 \AA , based on the repeat unit of eight Mn atoms (Figure 3b). These 1D inorganic helices are interconnected by ip^{2-} anions to constitute a complicated I^1O^2 type 3D framework (Figure 3a).

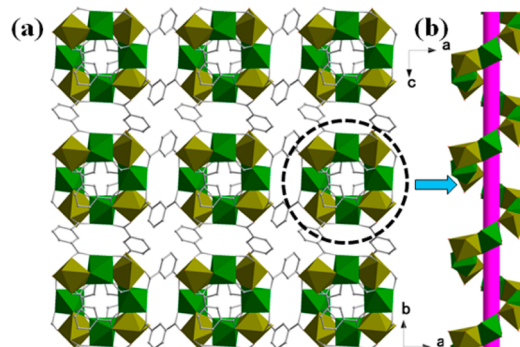


Figure 3. (a) View of 3D structure of **2P**. (b) View of the 1D helical $Mn-O-Mn$ inorganic connectivity in **2P**.

The H_2ip ligand and its derivatives have long been used to construct metal–organic frameworks with helical structures. Owing to its 120° bite angle and “partial flexibility”, the H_2ip ligand may play an important role in the helicity induction and maintenance of the framework.²² In **2P**, each ip^{2-} ligand connects two Mn^{II} atoms at both ends resulting in a $Mn2-ip^{2-}$ helical strand with a pitch of 56.434 \AA (Figure 4a). Five such identical helical chains are extended along the c axis to form a 5-fold right-handed helix (Figure 4b and S5b, Supporting Information). Every 5-fold helix is intertwined with four others to produce an unprecedented entangled motif of **2P** (Figure 4c). From the topological point of view, the ip^{2-} ligand and the bridging fragment of Mn1 ($Mn2-Mn1-Mn2$) can be viewed as connectors and Mn2 as a node (Supporting Information, Figure S6a). Therefore, the 3D framework of **2P** can be abstracted into a 6-connected network with the Schläfli symbol of $3^3\cdot 4^2\cdot 5\cdot 6^6\cdot 7^3$ (Supporting Information, Figure S6b). It should be pointed out that, even through the single crystal of **2** is chiral, the bulk sample of **2** is a racemic mixture, as confirmed by CD experiments (Supporting Information, Figure S7).

Crystal Structure of $[Mn_2(OH-ip)_2(DMF)]\cdot DMF$ (3). The asymmetric unit of **3** consists of three Mn^{II} ions, two OH-ip²⁻ anions, and one coordinated and one guest DMF molecule (Supporting Information, Figure S8). The crystallographically

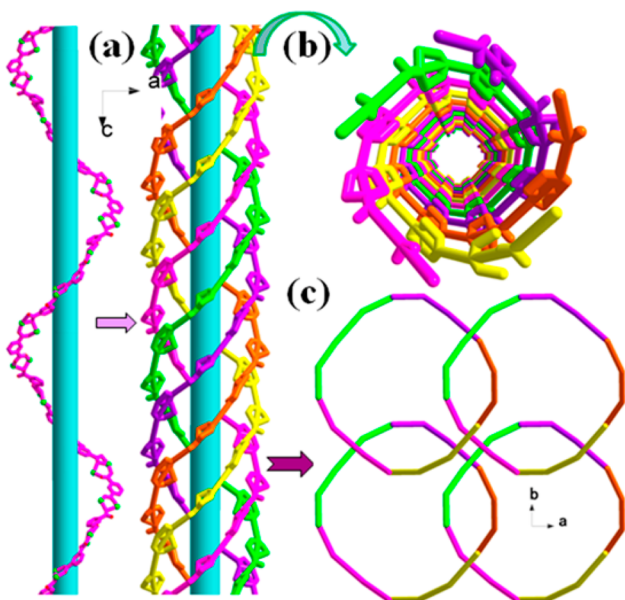


Figure 4. (a) View of the right-handed single helix in **2P**. (b) View of the right-handed 5-fold helix in **2P**. (c) View of the 3D framework of **2P** constructed by right-handed 5-fold helices.

independent Mn1, Mn2, and Mn3 have 1, 1/2, and 1/2 site occupancies, respectively. The Mn1 ion is surrounded by five carboxylate oxygen atoms and one DMF oxygen atom, Mn2 is coordinated by six carboxylate oxygen atoms, and Mn3 is coordinated by four carboxylate oxygen atoms and two DMF oxygen atoms (Figure 1c). Each Mn3 octahedron shares a corner with a Mn1 octahedron on both sides, which in turn edge-shares with a Mn2 octahedron, generating an infinite zigzag-like inorganic chain $\{\text{Mn}_1-\text{Mn}_3-\text{Mn}_1-\text{Mn}_2\}_n$ aligned parallel to the *b* axis (Figure 5a). In the inorganic chain, the

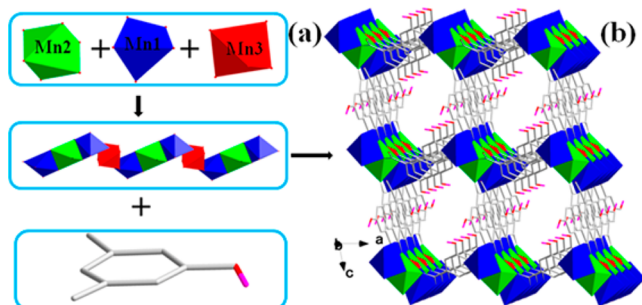


Figure 5. (a) View of the polyhedra of Mn1, Mn2, Mn3, and 1D inorganic Mn–O–Mn connectivity in **3**. (b) View of the 3D structure of **3** with I^1O^2 hybrid type.

distances of $\text{Mn}_1\cdots\text{Mn}_2$ and $\text{Mn}_1\cdots\text{Mn}_3$ are 3.46 and 3.53 Å. These 1D chains are further connected by two types of OH-ip²⁻ ligands (one coordinates to four Mn atoms in a bidentate bridging mode while the other adopts a ($k^1\text{-}\mu_2$)-($k^2\text{-}\mu_2$)- μ_5 bridging mode) to form a 3D I^1O^2 architecture (Figure 5b). From the topological point of view, $\text{Mn}_1-\text{Mn}_1\text{C}$, $\text{Mn}_1-\text{Mn}_1\text{E}$, and OH-ip²⁻ ligands can be regarded as connectors while Mn1 as a node. Thus, the 3D framework of **3** can be simplified as a five-connected framework with **bnn** topology (Supporting Information, Figure S9).

Crystal Structure of $(\text{Me}_2\text{NH}_2)[\text{Mn}_4(\text{sdba})_4(\text{Hsdba})(\text{H}_2\text{O})]\cdot 3\text{H}_2\text{O}\cdot 2\text{DMF}$ (4). Compound **4** crystallizes in the

monoclinic acentric space group *Cc*. Its asymmetric unit contains four crystallographically independent Mn^{II} ions, which are all six-coordinate and adopt an octahedral geometry (Supporting Information, Figure S10). The Mn1 and Mn4 are surrounded by one water molecule and five carboxylate oxygen atoms, while Mn2 and Mn3 are each coordinated by six carboxylate oxygen atoms (Figure 1d). The Mn–O bond lengths range from 2.064(4) to 2.505(5) Å, and the Mn···Mn distances vary from 3.52(7) to 3.72(2) Å. The O–Mn–O cis angles lie in the range 54.49(1)–179.02(1)°, showing high distortion of the Mn^{II} octahedral geometry. The Mn_1O_6 , Mn_2O_6 , Mn_3O_6 , and Mn_4O_6 polyhedra are connected in order one by one via corner-sharing oxygen atoms, O5, O6, and O14C, respectively, to generate a Mn1–Mn2–Mn3–Mn4 unit. This unit shares two edges (O13C···O31D and O13A···O31) with the symmetry-related Mn1D and Mn4E polyhedra to form a 1D inorganic Mn–O–Mn sawtooth-like chain (Figure 6a).

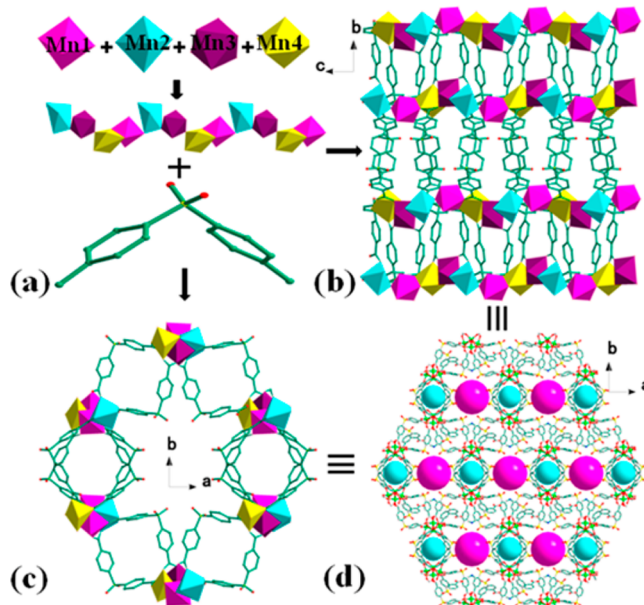


Figure 6. (a) View of the polyhedra of Mn1, Mn2, Mn3, Mn4, and 1D inorganic Mn–O–Mn connectivity in **4**. (b), (c) View of the 3D structure of **4** from the *a* and *c* axes. (d) View of the 3D microporous framework of **4**. The $(\text{Me}_2\text{NH}_2)^+$ cations were omitted for clarity.

These infinite chains are then cross-linked by sdba²⁻ and Hsdba⁻ ligands to create the ultimate microporous framework with I^1O^2 hybrid connectivity (Figure 6b–d). PLATON²⁰ analysis shows that the effective free volume of **4** is 35.9% of the crystal volume (3703.5 Å out of the 10310.0 Å unit cell volume). From the topological point of view, the carboxylate ligands, and the bridging fragments of Mn1 (Mn1–Mn4E) and Mn4 (Mn4–Mn1D), can be treated as connectors while the {Mn1–Mn2–Mn3–Mn4} unit acts as a node. Thus, the overall 3D framework of **4** can be abstracted into a 6-connected **sxd** net with the Schläfli symbol of $3^3\cdot 4^6\text{S}^5\cdot 6$ (Supporting Information, Figure S11).

Thermal Characterization. To investigate the thermal stability of **1–4**, thermal analyses have been carried out on crystalline samples in a nitrogen atmosphere (Supporting Information, Figure S12). The TGA curve of **1** indicates that there is a weight loss of 9.00% from 40 to 190 °C, which can be attributed to the loss of three water molecules (calcd =

11.50%). Upon further heating, a steady plateau up to 348 °C was observed, from which **1** starts to decompose. The curve of **2** exhibits a two-step mass loss. The first step from 40 to 140 °C corresponds to the loss of a lattice CH₃OH molecule (obsd = 6.61%, calcd = 6.57%). The second weight loss occurs over the range of 140–380 °C relevant to the release of one coordinated H₂O molecule (obsd = 3.69%, calcd = 4.26%). Above 380 °C the framework of **2** decomposes gradually. For **3**, it is stable up to about 130 °C, from which to 354 °C occurs the weight loss corresponding to the release of free and coordinated DMF molecules (obsd = 24.25%, calcd = 23.72%). The TGA curve of **4** indicates that there are two steps of mass loss. The first weight loss from 40 to 150 °C can be attributed to the loss of coordinated and free H₂O molecules (obsd = 3.64%, calcd = 3.59%). The second weight loss from 150 to 317 °C may be due to the release of free DMF molecules (obsd = 7.69%, calcd = 7.29%). From 317 °C the framework of **4** begins to decompose.

Magnetic Property of 1. The magnetic susceptibility data of **1** is shown in Figure 7. At 300 K, the $\chi_m T$ is 4.22 cm³ mol⁻¹

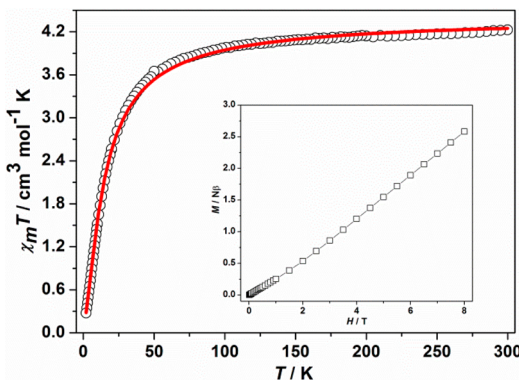


Figure 7. Plots of $\chi_m T$ vs T in the 2–300 K temperature range for **1**. Inset: plot of M vs H for **1**. The red solid line represents the best theoretical fit.

K, which is very close to the value of 4.375 cm³ mol⁻¹ K for an isolated Mn^{II} ion with $g = 2.0$. The $\chi_m T$ decreases continuously with decreasing temperature and reaches a minimum value of 0.26 cm³ mol⁻¹ K at 2 K. This behavior is indicative of antiferromagnetic (AF) interaction in **1**, as suggested by the negative Weiss Constant $\theta = -10.35$ K, obtained from the data of $1/\chi_m$ versus T in the temperature range 20–300 K by the Curie–Weiss law (Supporting Information, Figure S13a). The magnetization increases linearly with increasing magnetic field, and reaches a value of 2.58 $N\beta$ at 8 T, which is lower than the

saturation value of one Mn^{II} ion ($5 N\beta$ for $g = 2.0$), suggesting again the AF interaction in **1** (Figure 7, insert).

To determine the exchange coupling between the adjacent Mn^{II} ions mediated via double *syn–anti* carboxylate bridges, $\chi_m T$ data were fitted by using the infinite-chain model (Scheme 1a) of classical spins derived by Fisher with $H = -J \sum S_i S_{i+1}$ (J stands for the exchange constant between the adjacent Mn^{II} ions, and S_i are the classical spin vectors).²³ The corresponding analytical expression for the product is as follows:

$$\chi_m = [Ng^2\beta^2S(S+1)/3KT][(1+u)/(1-u)] \quad (1)$$

Here, $u = \coth(JS(S+1)/KT) - KT/JS(S+1)$, where N , g , β , and K have their usual meanings. Due to carboxylate groups or inorganic oxygen atoms in the inorganic chain mediating stronger magnetic interactions than the benzene rings among the chains, the magnetic exchanges between adjacent chains are thus not considered. The best fit in the whole temperature range gives $g = 2.00$, $J = -1.32$ cm⁻¹, and $R = 2.1 \times 10^{-3}$. The fitting result also reveals weak AF interaction between the Mn^{II} centers.

To the best of our knowledge, so far only five Mn^{II}–carboxylate chains related to **1** have been structurally and magnetically characterized.^{13c,21} Selected structural parameters and J values of them including those of **1** are collected in Table 2. It can be found that the double *syn–anti* bridge seems to induce weak antiferromagnetic coupling between the Mn^{II} ions with J values ranging from -0.89 to -1.8 cm⁻¹. Compounds **II**, **III**, and **1** show similar J values, which is in accordance with the similarity of their structural parameters. Similar behavior is also observed for **IV** and **V**. It is interesting to compare compounds **I** and **V**, which have almost the same structural parameters but different degree of magnetic coupling. Since magnetic properties are also affected by electron-withdrawing ability of the substituent groups bonded to the carboxylate bridges, the difference in magnitude of magnetic coupling in **I** and **V** should be attributed to the different electron-withdrawing ability of the substituent group R of the ligands ($R = \text{CH}_2\text{Cl}$ in **I**, $R = \text{C}_6\text{H}_4\text{Cl}$ in **V**).

Magnetic Property of 2. The $\chi_m T$ curve of **2** is shown in Figure 8. At room temperature, the $\chi_m T$ value is shown to be 4.10 cm³ mol⁻¹ K, which is lower than the expected value for one magnetically isolated high-spin Mn^{II} ion. Upon cooling, the $\chi_m T$ value decreases smoothly and reaches a value of 0.22 cm³ mol⁻¹ K at 2 K. The magnetic susceptibility data can be fitted to the Curie–Weiss law in the temperature range 30–300 K with $\theta = -37.54$ K, indicating overall AF interaction in **2** (Supporting Information, Figure S13b). The magnetization increases linearly with increasing magnetic field and reaches a

Table 2. Structural and Magnetic Parameters for 1D Mn^{II}–Carboxylate Systems with Double *syn–anti* Bridges

complex ^a	no.	d_{syn}^b (Å)	d_{anti}^c (Å)	τ^d (deg)	Mn–Mn (Å)	J^e (cm ⁻¹)	ref
[Mn(L1) ₂ (phen)]	I	2.13	2.18	42.14	4.53	-0.89	21c
[MnL2(bpy)]	II	2.16	2.16	51.17	4.79	-1.04	21a
[Mn(L3) ₂]	III	2.15	2.20	50.87	4.61	-1.28	21b
[Mn(Am-Hip) ₂]·3H ₂ O	1	2.17	2.18	50.88	4.54	-1.32	this work
[Mn(L4) ₂ (bpy)]·H ₂ O	IV	2.11	2.20	43.90	4.52	-1.72	21d
[Mn(L4) ₂ (phen)]	V	2.09	2.20	43.51	4.50	-1.80	13c

^aAbbreviation: HL1 = chloroacetic acid, Na₂L2 = 2,3-bis(carboxyl)-6,7-bimethylthio-tetrathiafulvalene sodium salt, HL3 = 3-aminobenzoic acid, HL4 = 3-chlorobenzoic, phen = 1, 10-phenanthroline, bpy = 2,2'-bipyridine. ^bThe average value of Mn–O_{syn} bond lengths. ^cThe average value of Mn–O_{anti} bond lengths. ^dThe average torsion angle of Mn–O–C–O. ^eThe 2J scheme in the exchange coupling Hamiltonian was converted to the J scheme for comparison.

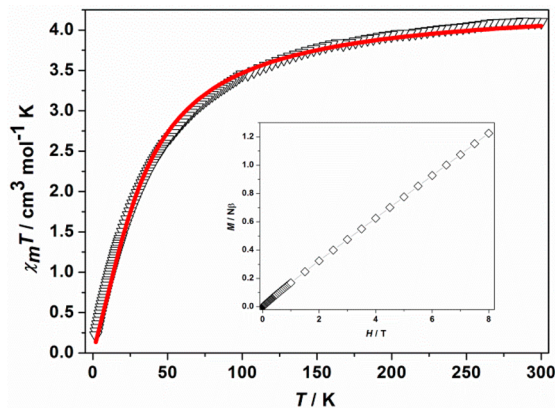


Figure 8. Plots of $\chi_m T$ vs T in the 2–300 K temperature range for 2. Inset: Plot of M vs H for 2. The red solid line represents the best theoretical fit.

value of $1.23 N\beta$ at 8 T, which is lower than the saturation value of one Mn^{II} ion ($5 N\beta$ for $g = 2.0$), suggesting again the AF interaction (Figure 8, insert).

On the basis of magnetic topology, the Mn^{II} ions in the inorganic Mn–O–Mn helical chain of 2 are alternately bridged by a single μ_2 -O bridge (from a μ_3 -carboxylate group) and a double μ_2 -O bridge (from a k^1, μ_2 - and μ_3 -carboxylate group, respectively) (Scheme 1b). The coupling transferred between Mn1 and Mn1D (or Mn2 and Mn2D) can be neglected due to their long Mn···Mn distance ($\text{Mn1} \cdots \text{Mn1D} = 5.52(7)$, $\text{Mn2} \cdots \text{Mn2D} = 6.76(4)$ Å) (Figure 1b). Thus, the magnetic exchange pathway within the helical chain can be described as a magnetic Mn^{II} chain with a periodically alternating $-J_1 J_2 J_1 J_2 -$ coupling sequence. To simulate the experimental magnetic behavior, the theoretical model proposed by Rojo et al. for an alternating $-J_1 J_2 J_1 J_2 -$ chain with $S = 5/2$ was used.^{5a} The nearest-neighbor exchange interactions are described by the following Hamiltonian (eq 2):

$$H = \sum -[J_1 S_{2i} S_{2i+1} + J_2 S_{2i+1} S_{2i+2}] \quad (2)$$

The deduced expression of the molar susceptibility χ_m is

$$\chi_m = [Ng^2 \beta^2 S(S+1)/3KT][(1+u_1+u_2+u_1u_2)/(1-u_1u_2)] \quad (3)$$

$$u_i = \coth(J_i S(S+1)/KT) - KT/J_i S(S+1) \quad (i = 1, 2) \quad (4)$$

The experimental data were fitted in the whole temperature range by eqs 3 and 4, leading to the best fit parameters of $J_1 = -4.35 \text{ cm}^{-1}$, $J_2 = -0.94 \text{ cm}^{-1}$, $g = 1.99$, and $R = 6.58 \times 10^{-3}$. This numerical analysis only gives us the magnitude of the two exchange parameters J_1 and J_2 but does not distinguish them. It has been known that, in general, the *syn-syn* carboxylate bridge mediates antiferromagnetic interaction, and the μ_2 -O bridge mediates ferromagnetic coupling only when the magnetic orbitals of the two metal atoms are nearly orthogonal; i.e., Mn–O–Mn bond angle is close to 90° .²⁴ Therefore, the superexchange pathway between the nearest-neighbor Mn^{II} ions in the helical chain of 2 depends on the cooperation effect of the *syn-syn* carboxylate and μ_2 -O bridges. As shown in Figure 1b, in addition to a *syn-syn* carboxylate bridge that mediates antiferromagnetic coupling, there are two μ_2 -O bridges between Mn1 and M2D: Mn1–O2D–Mn2D

(88.05°) and Mn1–O3C–Mn2D (97.79°). The former may mediate ferromagnetic coupling whereas the latter may mediate antiferromagnetic coupling. Thus, the overall coupling between Mn1 and M2D should be weakly antiferromagnetic. For Mn1–Mn2, there are two *syn-syn* carboxylate bridges and one μ_2 -O bridge ($\text{Mn1} \cdots \text{O1} \cdots \text{Mn2} = 100.66^\circ$), all of which can mediate antiferromagnetic coupling. As a result, compared to Mn1–Mn2D, a stronger antiferromagnetic coupling can be expected for Mn1–Mn2. Accordingly, J_1 represents the interaction of $\text{J}_{\text{Mn1}-\text{Mn2}}$ while J_2 stand for the coupling of $\text{J}_{\text{Mn1}-\text{Mn2D}}$. The J_1 and J_2 values are comparable to those previously reported for Mn^{II} chains or dimers with similar carboxylato bridging modes.

Magnetic Property of 3. The temperature dependence of magnetic susceptibility for 3 per Mn^{II} is shown in Figure 9. The

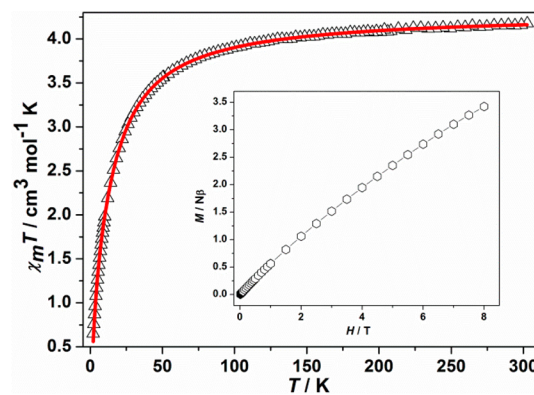


Figure 9. Plots of $\chi_m T$ vs T in the 2–300 K temperature range for 3. Inset: plot of M vs H for 3. The red solid line represents the best theoretical fit.

experimental $\chi_m T$ value at 300 K is $4.18 \text{ cm}^3 \text{ mol}^{-1} \text{ K}$, which is slightly smaller than the expected value for noninteracting high-spin Mn^{II} ions. As the temperature decreases, the χ_m value undergoes a monotonic decrease and reaches a minimum value of $0.65 \text{ cm}^3 \text{ mol}^{-1} \text{ K}$ at 2 K, indicating a dominant AF coupling between the magnetic centers. Between 2 and 300 K, the χ_m follows the Curie–Weiss law with $\theta = -11.28$ K. The negative value of Weiss constant also confirms AF interaction (Supporting Information, Figure S13c). The magnetization versus field curve at 2 K is far from saturation, reaching $3.42 N\beta$ per Mn^{II} at 8 T, which is less than the expected saturation value of $5 N\beta$ for one Mn^{II} ion with $S = 5/2$ and $g = 2.0$, and is consistent with the presence of AF interactions in 3 (Figure 9, insert).

The Mn^{II} ions in the inorganic Mn–O–Mn zigzag chain of 3 are alternately bridged by a double μ_2 -O bridge (from a k^2, μ_2 - and a k^1, μ_2 -carboxylate group, respectively) and a single μ_2 -O bridge from a DMF molecule (Scheme 1c). Therefore, the magnetic exchange pathway within this 1D chain can be described as a magnetic Mn^{II} chain with a periodically alternating $-J_1 J_2 J_1 J_2 -$ coupling sequence. To evaluate the superexchange interactions of adjacent Mn^{II} ions, the infinite 1D chain model with a $-J_1 J_2 J_1 J_2 -$ magnetic sequence was used.^{7a,25} The spin Hamiltonian of this alternating sequence is

$$H = \sum -[J_1 S_{4i+1} S_{4i+2} + J_1 S_{4i+2} S_{4i+3} + J_2 S_{4i+3} S_{4i+4} + J_2 S_{4i+4} S_{4i+5}] \quad (5)$$

The magnetic susceptibility is given by eq 6

$$\chi_m = [Ng^2S(S+1)/12KT][D/(1-u_1^2u_2^2)] \quad (6)$$

where $D = 4 + 4u_1 + 4u_2 + 2u_1^2 + 2u_2^2 + 4u_1u_2 + 4u_1^2u_2 + 4u_1u_2^2 + 4u_1^2u_2^2$, $u_1 = \coth(J_1S(S+1)/KT) - KT/J_1S(S+1)$, and $u_2 = \coth(J_2S(S+1)/KT) - KT/J_2S(S+1)$. The best-fitting parameter in the whole temperature range gives $J_1 = -2.66 \text{ cm}^{-1}$, $J_2 = -0.63 \text{ cm}^{-1}$, $g = 1.98$, and $R = 2.1 \times 10^{-4}$. Like 2, this numerical analysis also cannot distinguish between J_1 and J_2 . As discussed above, a stronger antiferromagnetic coupling for Mn1–Mn3 compared with that for Mn1–Mn2 can be expected because, in the latter case, the antiferromagnetic coupling was somewhat compensated by the ferromagnetic coupling caused by $\mu_2\text{-O}_2$ ($\text{Mn1-O}_2\text{-Mn2} = 91.49(2)^\circ$).^{24,26} Thus, the value for $J_{\text{Mn1-Mn3}}$ should be -2.66 cm^{-1} , and that for $J_{\text{Mn1-Mn2}}$ should be -0.63 cm^{-1} . In 3, the values of J_1 and J_2 were all negative, and an antiferromagnetic state was gained. However, if J_1 and J_2 have opposite signs, a fascinating homometallic ferrimagnetic state can be expected, as first observed in $\{[\text{Mn}_4(\text{Bu}^t\text{-ip})_4(\text{CH}_3\text{OH})_2] \cdot (\text{H}_2\text{O})_2\}_{10d}$ ($\text{Bu}^t\text{-H}_2\text{ip} = 5\text{-tert-butyl-1,3-benzenedicarboxylate}$).

Magnetic Property of 4. The variable-temperature magnetic susceptibility data of 4 is shown in Figure 10. The

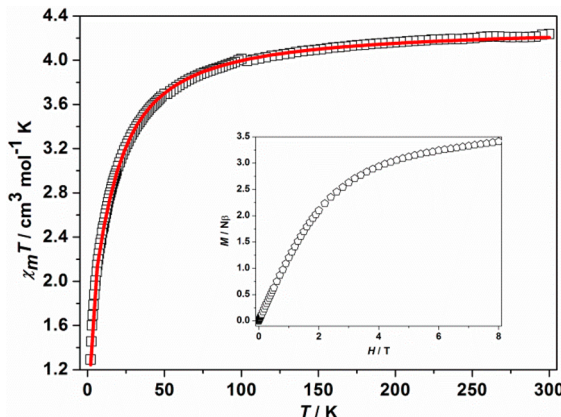


Figure 10. Plots of $\chi_m T$ vs T in the 2–300 K temperature range for 4. Inset: plot of M vs H for 4. The red solid line represents the best theoretical fit.

$\chi_m T$ value at 300 K is $4.24 \text{ cm}^3 \text{ mol}^{-1} \text{ K}$, which is somewhat lower than the expected value for one magnetically isolated high-spin Mn^{II} ion with $g = 2$ ($4.375 \text{ cm}^3 \text{ mol}^{-1} \text{ K}$). As the temperature decreases, the $\chi_m T$ value decreases monotonically, indicating an AF interaction operative between the neighboring Mn^{II} ions. This antiferromagnetic behavior is further confirmed by the negative Weiss constant $\theta = -8.55 \text{ K}$ (obtained by fitting the reciprocal magnetic susceptibility ($1/\chi_m$) to the Curie–Weiss law above 10 K, Supporting Information Figure S13d). The magnetization value reaches $3.40 \text{ N}\beta$ per Mn^{II} at 8 T, which is less than the expected saturation value of $5 \text{ N}\beta$ for one Mn^{II} ion with $S = 5/2$ and $g = 2.0$. At low field, the magnetization increases linearly with increasing magnetic field, which is in accordance with the presence of antiferromagnetic interaction (Figure 10, inset).

The oxygen bridges between the Mn^{II} ions in the 1D inorganic Mn–O–Mn chain of 4 can be divided into two sets alternately presented in the ratio of 1:3 (Scheme 1d). One connects Mn4E and Mn1 by a double $\mu_2\text{-O}$ bridge; the other links Mn1 and Mn2, Mn2 and Mn3, Mn3 and Mn4 through a single $\mu_2\text{-O}$ bridge (Figure 1d). At first glance, it seems that this

magnetic chain can be simplified as $-J_1J_2J_2-$ coupling sequence. Nevertheless, the Mn2–O6–Mn3 (108.34°) and Mn3–O14C–Mn4 (107.40°) angles are nearly the same, but both larger than the Mn1–O5–Mn2 (98.38°) angle. Therefore, to be more precise, the magnetic exchange pathways within the chain should be described as a magnetic Mn^{II} chain with periodically alternating $-J_1J_2J_3-$ coupling sequence. It is worth noting that the alternating $-J_1J_2-$ and $-J_1J_2J_2-$ magnetic chain's sequences have been observed in some reported Mn^{II} compounds, but the alternating $-J_1J_2J_3-$ magnetic sequence presented in 4 has never been reported and is a new type of magnetic chain sequence. The spin Hamiltonian of such a sequence can be written as

$$H = \sum -[J_1S_{4i+1}S_{4i+2} + J_2S_{4i+2}S_{4i+3} + J_3S_{4i+3}S_{4i+4} + J_3S_{4i+4}S_{4i+5}] \quad (7)$$

To our knowledge, no analytical law for such alternating sequence is available prior to this study. Fortunately, the large value of the local spin moment for Mn^{II} ions can be viewed as classical spin moments, i.e., as vectors. An exact methodology for describing the magnetic behavior of 1D classical chain was deduced by Fisher.²³ Abu-Youssef^{6a,9} and others^{5a,7a,8,25} later extended this methodology to the regular alternating 1D chains. Following the latter methodology and the interaction topology above, the expression of bulk susceptibility for this type of spin topology can be deduced.

$$\chi_m = [Ng^2S(S+1)/12KT][D/(1-u_1u_2u_3^2)] \quad (8)$$

Here $u_i = \coth(J_iS(S+1)/KT) - KT/J_iS(S+1)$ ($i = 1, 2$, and 3), and $D = 4 + 2u_1 + 2u_2 + 4u_3 + 2u_1u_2 + 4u_2u_3 + 2u_3^2 + 4u_1u_2u_3 + 2u_1u_3^2 + 2u_2u_3^2 + 4u_1u_2u_3^2$. In order to check the validity of eq 8, we verified that this equation can be reduced to eq 1 when $u_1 = u_2 = u_3$, and to eq 6 when $u_1 = u_2$.

The best fit of the experimental magnetic data over the whole temperature range gives $J_1 = -0.56 \text{ cm}^{-1}$, $J_2 = -2.82 \text{ cm}^{-1}$, $J_3 = -0.04 \text{ cm}^{-1}$, $g = 1.99$, and $R = 2.6 \times 10^{-4}$. The negative J_1 , J_2 , and J_3 values indicate AF interaction between the adjacent Mn^{II} ions.

Magneto-Structural Study of 1D Alternating Mn^{II} -Carboxylate Chains. The bis(*syn-syn*)/ $\mu_2\text{-O}$ and (*syn-syn*)/bis($\mu_2\text{-O}$) mixed bridging pathways presented in 2, 3, and 4 have also been observed in some other Mn^{II} -carboxylate compounds reported elsewhere.^{10c-e,11b-d} The compounds with available data of magnetic exchange are compiled in Table 3, which also includes the relevant magnetostructural data. All of these compounds are chain-based compounds, of which A, B, D, and E each contains a 1D uniform chain ($J_1J_2J_1$) with a bis(*syn-syn*)/ $\mu_2\text{-O}$ bridge, while the rest (C, F, and G) contain 1D chains with alternating bis(*syn-syn*)/ $\mu_2\text{-O}$ and (*syn-syn*)/bis($\mu_2\text{-O}$) bridges (J_1J_2 for C, $J_1J_2J_2$ for F and G). Whatever the type of chains is, it is obvious that the bis(*syn-syn*)/ $\mu_2\text{-O}$ bridge is easy to induce AF interaction with the coupling constants ranging from -0.04 to -4.35 cm^{-1} . It is known that the magnetic interaction through *syn-syn* carboxylato bridging pathway is usually weak and antiferromagnetic, while for $\mu_2\text{-O}$, ferro- or antiferromagnetic coupling occurs depending on the Mn–O–Mn angles. Therefore, the overall nature of the magnetic interaction of bis(*syn-syn*)/ $\mu_2\text{-O}$ bridging pathway could be determined by the competitive effect of the two exchange pathways, and the magnitude of the magnetic coupling may be affected by the pertinent structure parameters

Table 3. Structural and Magnetic Parameters for Bis(*syn-syn*)/ μ_2 -O and (*syn-syn*)/Bis(μ_2 -O) Bridges for Mn^{II}-Carboxylate Chain Compounds

complex ^a	no.	$d_{\mu_2\text{-O}}^b$ (Å)	d_{syn}^c (Å)	τ^d (deg)	Mn···Mn (Å)	Mn–O–Mn ^e (deg)	$ J $ (cm ⁻¹)	ref
Bis(<i>syn-syn</i>)/ μ_2 -O								
(Me ₂ NH ₂) ₂ [Mn ₄ (L1) ₄ (HL1)(H ₂ O)]·Solv	4 ^g	2.29	2.10	22.4	3.70	107.9	-0.04	this work
Mn ₂ (L2) ₂ (DMA) ₂	A	2.28	2.14	31.1	3.80	112.8	-1.16	11c
[Mn ₂ (L3)(H ₂ O)(DMA)]·DMA	B	2.28	2.14	6.6	3.73	109.3	-2.14	11d
[Na{Mn ₃ (HL4) ₂ (L)}·SH ₂ O]	C	2.22	2.17	15.3	3.48	103.7	-2.40	11b
[Mn ₂ (L3)(H ₂ O)(NMP)]·NMP	D	2.29	2.14	7.4	3.75	110.4	-2.56	11d
[Mn ₂ (L5) ₂ (DMF)]·DMF	3	2.33	2.14	23.2	3.53	98.3	-2.66	this work
(Me ₂ NH ₂) ₂ [Mn ₄ (L1) ₄ (HL1)(H ₂ O)]·Solv	4 ^g	2.33	2.15	26.5	3.53	98.4	-2.82	this work
[Mn ₂ (L6)(H ₂ O)]	E	2.30	2.15	26.7	3.53	100.1	-3.69	11b
[Mn ₄ (L7) ₄ (bip)]·2H ₂ O	F	2.30	2.16	11.2	3.55	100.8	-4.15	10e
[Mn ₄ (L7) ₄ (CH ₃ OH) ₂]·(H ₂ O) ₂	G	2.32	2.16	27.8	3.50	97.6	-4.31	10d
[Mn ₂ (L8) ₂ (H ₂ O)]·CH ₃ OH	2	2.23	2.18	20.9	3.43	100.7	-4.35	this work
(<i>syn-syn</i>)/Bis(μ_2 -O)								
[Mn ₄ (L7) ₄ (bip)]·2H ₂ O	F	2.30	2.11	28.7	3.20	88.4	-0.15	10e
[Mn ₄ (L7) ₄ (CH ₃ OH) ₂]·(H ₂ O) ₂	G	2.28	2.13	21.7	3.35	91.0	0.11	10d
(Me ₂ NH ₂) ₂ [Mn ₄ (L1) ₄ (HL1)(H ₂ O)]·Solv	4	2.35	2.10	5.36	3.57	98.6	-0.56	this work
Na{Mn ₃ (HL4) ₂ (L4)}·SH ₂ O	C	2.27	2.10	6.50	3.41	97.4	-0.60	11b
[Mn ₂ (L5) ₂ (DMF)]·DMF	3	2.31	2.11	6.34	3.46	97.2	-0.63	this work
[Mn ₂ (L8) ₂ (H ₂ O)]·CH ₃ OH	2	2.35	2.08	20.5	3.38	92.1	-0.96	this work

^aAbbreviation: H₂L1 = 4,4'-sulfonyldibenzoic acid, H₂L2 = 2,5-thiophenedicarboxylic acid, H₄L3 = [1,1':4',1"-terphenyl]-2',4,4",5'-tetracarboxylic acid, H₂L4 = 1,3,5-benzene tricarboxylic acid, H₂L5 = 5-hydroxyisophthalic acid, H₂L6 = diethylmalonate, H₂L7 = 5-*tert*-butyl-1,3-benzenedicarboxylate, H₂L8 = isophthalic acid, bip = 1,3-bis(imidazol)propane. ^bThe average value of Mn–O _{μ_2 -O} bond distance. ^cThe average value of Mn–O_{syn} bond lengths. ^dThe average torsion angle of Mn–O–C–O. ^eThe average value of Mn–O–Mn. ^fvalues reported here correspond to the convention $H = -JS_aS_b$ for nearest two coupled centers. ^gCompound 4 contains two sets of bis(*syn-syn*)/ μ_2 -O bridges with distinct structural parameters.

of both bridges, such as the Mn–O_{syn} and Mn–O _{μ_2 -O} bond lengths, the Mn–Mn distance, the Mn–O–Mn bond angles, and also the angular parameters of the carboxylate bridges.

As indicated in Table 3, the average Mn–O_{syn} bond lengths fall within a very narrow range 2.10–2.16 Å, and the average Mn–O _{μ_2 -O} bond lengths deviate slightly between 2.22 and 2.33 Å. In contrast, the Mn–O–Mn angles differ significantly. So the most relevant parameter that impacts the magnitude of the mixed pathway seems to be the Mn–O–Mn angle. The $|J|$ values are thus plotted against the Mn–O–Mn angles. The plot shows a trend that the antiferromagnetic interaction decreases as the bridging angle increases, though there is some degree of dispersion (Figure 11). There is also another trend that J decreases with the increasing of the Mn···Mn distance. This correlation is trivial because the Mn···Mn distance is mainly

determined by the Mn–O–Mn angle. For comparison, the Mn···Mn distances are also plotted against the Mn–O–Mn angles to illustrate the liner increase of Mn···Mn distances with the Mn–O–Mn angles. It has been well-documented that for Cu^{II} and Mn^{III/IV} complexes the magnetic coupling is dominated by the interaction between the d_{x²-y²} metal magnetic orbitals of two adjacent magnetic atoms via the oxo bridge.²⁷ For the Mn^{II} complexes, the metal x² – y² orbital is half-occupied and is aligned to allow overlap with the oxygen orbitals. The strength of overlap is affected by the Mn–O–Mn angle, which implies that this angle is a very important factor in the magnitude of the magnetic exchange coupling. For 1D inorganic–organic hybrid Mn^{II} complexes, the larger the Mn–O–Mn angle, the smaller the dx² – y²/dx² – y² interaction through the μ_2 -O bridge, and the lower the $|J|$ value.

As shown in Figure 11, there are some deviations from the linear trend. For example, in comparison with G, compound 2 exhibits a larger $|J|$ value but has a bigger Mn–O–Mn angle (Table 3). This deviation may be due to the variation of other parameters. If we take into account the contribution of average Mn–O–C–O torsion angle (τ) of the two *syn-syn* carboxylate bridges, this deviation can be well-illustrated. In general, a larger torsion angle of a *syn-syn* carboxylate bridge should disprove the magnetic interaction. Thus, the $|J|$ value of 2 ($\tau = 20.9^\circ$) is larger than that of G ($\tau = 27.8^\circ$) even though the latter has a smaller Mn–O–Mn bond angle than the former. Similarly, the smaller τ angle of F ($\tau = 11.2^\circ$) may be responsible for its larger $|J|$ value compared to E ($\tau = 26.7^\circ$). Since compounds B and D have essentially the same torsion angles, they exhibit almost the same $|J|$ values, and so do 3 and 4. Accordingly, compound 2 should exhibit a smaller $|J|$ value compared to F. However, they have nearly the same strength of interaction. This can be interpreted by considering the influence of electronegativity of

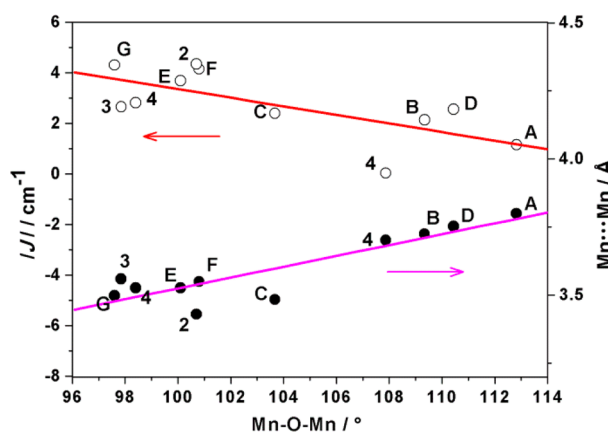


Figure 11. Coupling constants $|J|$ and Mn···Mn distances against the bridging Mn–O–Mn angles. The solid lines are just guides for the eye.

the carboxylate groups. Generally, an increase in electro-negativity of the carboxylate ligand reduces the antiferromagnetic coupling strength.^{13e,28} Consequently, the weaker electro-negativity of the carboxylate ligand of **2** in comparison with F may enhance the strength of interaction, which compensates for the decrease of $|J|$ caused by the large torsion angle. A similar situation was observed for **3** and **G**, which have similar Mn–O–Mn bond angles and τ , but with different electro-negativity of the carboxylate groups.

The (*syn*–*syn*)/bis(μ_2 -O) mixed bridge is rarely observed in the 1D Mn^{II}–carboxylate system, and only three examples are available in the literature. The structural and magnetic data are also listed in Table 3 together with those of **2**, **3**, and **4**. Considering the limited data, the magneto-structural correlation is difficult to derive. Nonetheless, Table 3 indicates that the interaction nature of these compounds is either AF coupling or ferromagnetic interaction in the range from 0.11 to -1.26 cm^{-1} , and is sensitive to the Mn–O–Mn bond angles. The Mn–O–Mn bond angle in **G** is close to 90° , which mediates ferromagnetic interaction.²⁴ Considering this, the weak ferromagnetic coupling of **G** may be caused by orbital counter complementarities between *syn*–*syn* and bis(μ_2 -O) carboxylate bridges that induce AF and ferromagnetic interactions, respectively ($J = J_{\text{AF}} + J_F$ with J_{AF} negative and J_F positive and $|J_{\text{AF}}| < |J_F|$). Compound **2** has a Mn–O–Mn bond angle approximately the same as that of **G**, yet exhibits a weak AF interaction. The smaller average Mn–O_{*syn*} bond length of **2** compared to **G** may lead to a stronger AF interaction ($|J_{\text{AF}}| > |J_F|$), resulting in an overall weak AF interaction. Other compounds also exhibit a weak AF coupling, which may be due to their small τ angles that enhance the AF contribution of the *syn*–*syn* carboxylate bridges, thus leading to an overall weak AF interaction.

EPR Spectra. The X-band spectra of **1**–**4** were recorded on powder samples at room temperature. The shape of the spectra of **1**–**4** is nearly the same: an isotropic signal band centered at $g \approx 2$ is observed, but with a different peak-to-peak line width of 209 G for **1**, 348 G for **2**, 560 G for **3**, and 290 G for **4** (Supporting Information, Figure S14a–d). For MOFs, it is difficult to interpret the origin of this difference, because many factors, such as the dipolar interaction, intrachain coupling, hyperfine coupling, or even single-ion ZFS effect can influence the line width of this system. However, considering the different magnitude of magnetic coupling and the degree of distortion of Mn^{II} coordination polyhedra in **1**–**4**, we suggest that both of these two factors may be responsible for the differences in the room temperature X-band EPR spectra.

SHG and Dielectric Properties. The second-order nonlinear optical properties of **2** and **4** were investigated qualitatively as they both crystallize in the noncentrosymmetric space groups ($P4_3$ and Cc , respectively). Approximate estimations were carried out on a pulsed Q-switched Nd:YAG laser at a wavelength of 1064 nm. The intensities of the green light (frequency-doubled output: $\lambda = 532\text{ nm}$) produced by the powder samples of **2** and **4** are about 0.6 and 0.9 times, respectively, of that produced by a potassium dihydrogen phosphate (KDP) powder (Supporting Information, Figure S15).

As compounds **2** (C_4) and **4** (C_s) belong to the 10 polar point groups (C_1 , C_s , C_2 , C_{2v} , C_3 , C_{3v} , C_4 , C_{4v} , C_6 and C_{6v}) that are associated with ferroelectric behavior,¹⁷ the ferroelectric measurements were performed on their powder samples. The P – E plots of **2** and **4** exhibit a banana shape (Supporting

Information, Figure S16), which could not support the presence of ferroelectric properties.²⁹ In order to confirm whether they have ferroelectric properties or not, temperature dependence of dielectric constants of **2** and **4** were further measured on a pellet sample with frequencies from 1 to 50 kHz (Figure 12). For **2**, the real components ϵ' of dielectric

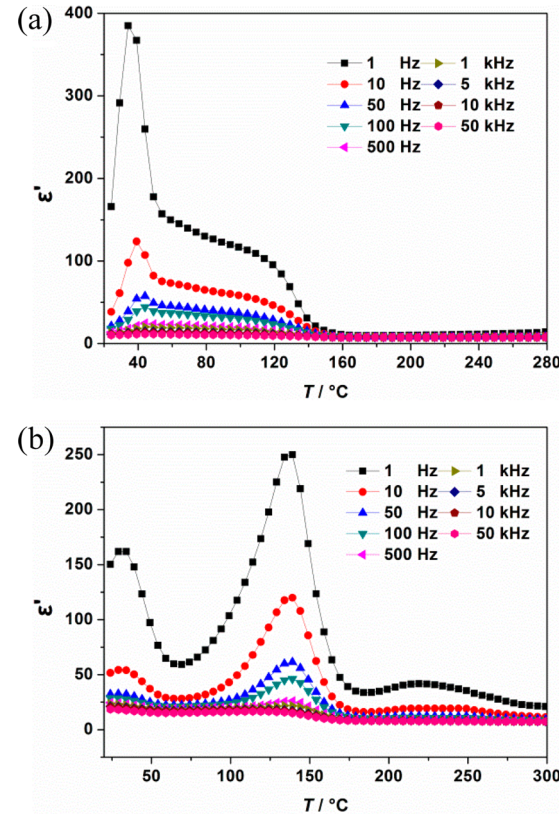


Figure 12. Temperature dependencies of the real part of the dielectric constants of **2** (a) and **4** (b) in the frequencies of 1–50 kHz.

constant exhibit one anomaly peak at about $35\text{ }^\circ\text{C}$. For **4**, three dielectric peaks at about 35, 140, and $220\text{ }^\circ\text{C}$ were observed. On the other hands, the TG curve of **2** (Supporting Information Figure S12) exhibits a weight loss nearly above room temperature, and thus, the dielectric anomaly at $35\text{ }^\circ\text{C}$ can be attributed to the weight loss of lattice CH_3OH molecules. Furthermore, considering the presence of free water, coordinated water, and free DMF molecules in **4**, the dielectric anomaly at 35, 140, and $220\text{ }^\circ\text{C}$ for **4** can be ascribed to the release of the free water, coordinated water, and DMF molecules, respectively, as indicated by the DSC curve (Supporting Information Figure S17). In a word, the dielectric anomaly in **2** and **4** was caused by the release of guest or coordinated solvent molecules, and the ferroelectric transition was not observed. Therefore, we suggest that the hysteresis loops observed at room temperature for **2** and **4** may result from the leakance or interface charge.²⁹

CONCLUSION

In summary, by using various polycarboxylate ligands, four new inorganic–organic hybrid Mn^{II} magnetic coordination polymers **1**–**4** were synthesized and characterized. Single-crystal X-ray structure determination reveals that **1** has a layer structure constructed by a carboxylate-bridged Mn^{II} chain with a uniform

$-J_1J_1J_1J_1-$ magnetic chain's sequence. Compound **2** possesses a 3D structure that is built from an unprecedented 5-fold $Mn_2^{ip^2-}$ helical chain, in which the single helix exhibits an alternating inorganic $-J_1J_2J_1J_2-$ magnetic chain's sequence. Compound **3** displays a 3D **bnn** network containing a 1D chain with a $-J_1J_2J_1J_2-$ magnetic chain's sequence. Compound **4** shows a 3D microporous framework based on a 1D chain with a newly observed $-J_1J_2J_3J_1-$ magnetic chain's sequence. The magneto-structural correlations of **1–4** together with other most related Mn^{II} -carboxylate chains reported in the literature were also investigated, and the results indicate that the magnitude of the magnetic coupling is mainly correlated to the Mn–O–Mn angle of the μ_2 -O bridge and the average Mn–O–C–O torsion angle of the *syn-syn* carboxylate bridge, and also affected by the electronegativity of the carboxylate ligands. In addition, compounds **2** and **4** crystallize in chiral and acentric space groups, respectively, and they both display noticeable SHG response and dielectric anomaly. This study demonstrates that polycarboxylate ligands are good ligands to construct chain-based magnetic materials with diverse magnetic chain's sequences that are theoretically and practically useful.

ASSOCIATED CONTENT

Supporting Information

X-ray crystallographic data in CIF format, additional figures, tables for selected bond lengths and angles, PXRD patterns, TGA curves, DSC curves, CD and IR spectra. This material is available free of charge via the Internet at <http://pubs.acs.org>.

AUTHOR INFORMATION

Corresponding Author

*E-mail: swdu@fjirsm.ac.cn.

Notes

The authors declare no competing financial interest.

ACKNOWLEDGMENTS

We thank the National Basic Research Program of China (973 Program, 2012CB821702), the National Natural Science Foundation of China (21233009 and 21173221), and the State Key Laboratory of Structural Chemistry, Fujian Institute of Research on the Structure of Matter, Chinese Academy of Sciences, for financial support.

REFERENCES

- (a) Cheetham, A. K.; Rao, C. N. R.; Feller, R. K. *Chem. Commun.* **2006**, 4780–4795. (b) Clemente-Leon, M.; Coronado, E.; Martí-Gastaldo, C.; Romero, F. M. *Chem. Soc. Rev.* **2011**, *40*, 473–497.
- (c) Tian, C.; Zhang, H.; Du, S. *CrystEngComm* **2014**, *16*, 4059–4068.
- (2) (a) Clerac, R.; Miyasaka, H.; Yamashita, M.; Coulon, C. *J. Am. Chem. Soc.* **2002**, *124*, 12837–12844. (b) Harris, T. D.; Bennett, M. V.; Clerac, R.; Long, J. R. *J. Am. Chem. Soc.* **2010**, *132*, 3980–3988.
- (c) Sun, H.-L.; Wang, Z.-M.; Gao, S. *Coord. Chem. Rev.* **2010**, *254*, 1081–1100.
- (3) (a) Georges, R.; Borrás-Almenar, J. J.; Coronado, E.; Curély, J.; Drillon, M. In *Magnetism: Molecules to Materials I*; Wiley-VCH Verlag GmbH & Co. KGaA: Weinheim, 2003; pp 1–47. (b) Zheng, Y.-Z.; Zheng, Z.; Chen, X.-M. *Coord. Chem. Rev.* **2014**, *258*, 1–15.
- (4) (a) Zeng, Y.-F.; Hu, X.; Liu, F.-C.; Bu, X.-H. *Chem. Soc. Rev.* **2009**, *38*, 469–480. (b) Escuer, A.; Esteban, J.; Perlepes, S. P.; Stamatatos, T. C. *Coord. Chem. Rev.* **2014**, *275*, 87–129.
- (5) (a) Cortes, R.; Drillon, M.; Solans, X.; Lezama, L.; Rojo, T. *Inorg. Chem.* **1997**, *36*, 677–683. (b) Gao, E. Q.; Cheng, A. L.; Xu, Y. X.; He, M. Y.; Yan, C. H. *Inorg. Chem.* **2005**, *44*, 8822–8835. (c) Yue, Y.-F.; Gao, E.-Q.; Fang, C.-J.; Zheng, T.; Liang, J.; Yan, C.-H. *Cryst. Growth Des.* **2008**, *8*, 3295–3301.
- (6) (a) Abu-Youssef, M. A. M.; Drillon, M.; Escuer, A.; Goher, M. A. S.; Mautner, F. A.; Vicente, R. *Inorg. Chem.* **2000**, *39*, 5022–5027. (b) Jia, Q.-X.; Tian, H.; Zhang, J.-Y.; Gao, E.-Q. *Chem.—Eur. J.* **2011**, *17*, 1040–1051.
- (7) (a) Wang, Y.-Q.; Jia, Q.-X.; Wang, K.; Cheng, A.-L.; Gao, E.-Q. *Inorg. Chem.* **2010**, *49*, 1551–1560. (b) Zhuang, G.-M.; Li, X.-B.; Wen, Y.-Q.; Tian, C.-Y.; Gao, E.-Q. *Eur. J. Inorg. Chem.* **2014**, 3488–3498.
- (8) Liu, F.-C.; Zeng, Y.-F.; Zhao, J.-P.; Hu, B.-W.; Bu, X.-H.; Ribas, J.; Cano, J. *Inorg. Chem.* **2007**, *46*, 1520–1522.
- (9) Cano, J.; Journaux, Y.; Goher, M. A. S.; Abu-Youssef, M. A. M.; Mautner, F. A.; Reiss, G. J.; Escuer, A.; Vicente, R. *New J. Chem.* **2005**, *29*, 306–314.
- (10) (a) Wang, R. H.; Gao, E. Q.; Hong, M. C.; Gao, S.; Luo, J. H.; Lin, Z. Z.; Han, L.; Cao, R. *Inorg. Chem.* **2003**, *42*, 5486–5488. (b) Zeng, M.-H.; Wu, M.-C.; Liang, H.; Zhou, Y.-L.; Chen, X.-M.; Ng, S.-W. *Inorg. Chem.* **2007**, *46*, 7241–7243. (c) Nadeem, M. A.; Craig, D. J.; Bircher, R.; Stride, J. A. *Dalton Trans.* **2010**, *39*, 4358–4362. (d) Tian, C.-B.; He, Z.-Z.; Li, Z.-H.; Lin, P.; Du, S.-W. *CrystEngComm* **2011**, *13*, 3080–3086. (e) Ma, L.-F.; Han, M.-L.; Qin, J.-H.; Wang, L.-Y.; Du, M. *Inorg. Chem.* **2012**, *51*, 9431–9442.
- (11) (a) Tian, C.-B.; Chen, R.-P.; He, C.; Li, W.-J.; Wei, Q.; Zhang, X.-D.; Du, S.-W. *Chem. Commun.* **2014**, *50*, 1915–1917. (b) Deniz, M.; Hernandez-Rodriguez, I.; Pasan, J.; Fabelo, O.; Canadillas-Delgado, L.; Vallejo, J.; Julve, M.; Lloret, F.; Ruiz-Perez, C. *CrystEngComm* **2014**, *16*, 2766–2778. (c) Tan, Y.-X.; He, Y.-P.; Zhang, Y.; Zheng, Y.-J.; Zhang, J. *CrystEngComm* **2013**, *15*, 6009–6014. (d) Zhou, X.; Liu, P.; Huang, W.-H.; Kang, M.; Wang, Y.-Y.; Shi, Q.-Z. *CrystEngComm* **2013**, *15*, 8125–8132. (e) Tian, C.-B.; Zhang, H.-B.; Peng, Y.; Xie, Y.-E.; Lin, P.; Li, Z.-H.; Du, S.-W. *Eur. J. Inorg. Chem.* **2012**, *4029*–4035. (f) Saines, P. J.; Jain, P.; Cheetham, A. K. *Chem. Sci.* **2011**, *2*, 1929–1939. (g) Saines, P. J.; Melot, B. C.; Seshadri, R.; Cheetham, A. K. *Chem.—Eur. J.* **2010**, *16*, 7579–7585.
- (12) (a) Durot, S.; Policar, C.; Pelosi, G.; Bisceglie, F.; Mallah, T.; Mahy, J. P. *Inorg. Chem.* **2003**, *42*, 8072–8080. (b) Iikura, H.; Nagata, T. *Inorg. Chem.* **1998**, *37*, 4702–4711.
- (13) (a) Li, W.; Barton, P. T.; Burwood, R. P.; Cheetham, A. K. *Dalton Trans.* **2011**, *40*, 7147–7152. (b) Gomez, V.; Corbella, M.; Font-Bardia, M.; Calvet, T. *Dalton Trans.* **2010**, *39*, 11664–11674. (c) Gomez, V.; Corbella, M. *Eur. J. Inorg. Chem.* **2009**, 4471–4482.
- (d) Li, W.; Jia, H.-P.; Ju, Z.-F.; Zhang, J. *Dalton Trans.* **2008**, 5350–5357. (e) Garcia-Couceiro, U.; Castillo, O.; Cepeda, J.; Lanchas, M.; Luque, A.; Perez-Yanez, S.; Roman, P.; Vallejo-Sanchez, D. *Inorg. Chem.* **2010**, *49*, 11346–11361. (f) Earl, L. D.; Patrick, B. O.; Wolf, M. O. *Inorg. Chem.* **2013**, *52*, 10021–10030. (g) Wang, X.; Liu, L.; Conato, M.; Jacobson, A. J. *Cryst. Growth Des.* **2011**, *11*, 2257–2263.
- (14) (a) Wang, C.; Zhang, T.; Lin, W. *Chem. Rev.* **2012**, *112*, 1084–1104. (b) Zhang, W.; Xiong, R.-G. *Chem. Rev.* **2012**, *112*, 1163–1195. (c) Serra-Crespo, P.; van der Veen, M. A.; Gobechiya, E.; Houthoofd, K.; Filinchuk, Y.; Kirschhoff, C. E. A.; Martens, J. A.; Sels, B. F.; De Vos, D. E.; Kapteijn, F.; Gascon, J. *J. Am. Chem. Soc.* **2012**, *134*, 8314–8317. (d) Hang, T.; Zhang, W.; Ye, H.-Y.; Xiong, R.-G. *Chem. Soc. Rev.* **2011**, *40*, 3577–3598. (e) Ha, Y.-G.; Everaerts, K.; Hersam, M. C.; Marks, T. J. *Acc. Chem. Res.* **2014**, *47*, 1019–1028.
- (15) (a) Lee, H. N.; Christen, H. M.; Chisholm, M. F.; Rouleau, C. M.; Lowndes, D. H. *Nature* **2005**, *433*, 395–399. (b) Rijnders, G.; Blank, D. H. A. *Nature* **2005**, *433*, 369–370.
- (16) (a) Tang, Y.-Z.; Zhou, M.; Huang, J.; Tan, Y.-H.; Wu, J.-s.; Wen, H.-R. *Inorg. Chem.* **2013**, *52*, 1679–1681. (b) Du, F.; Zhang, H.; Tian, C.; Du, S. *Cryst. Growth Des.* **2013**, *13*, 1736–1742. (c) Wen, L.; Zhou, L.; Zhang, B.; Meng, X.; Qu, H.; Li, D. *J. Mater. Chem.* **2012**, *22*, 22603–22609. (d) Duan, X.; Meng, Q.; Su, Y.; Li, Y.; Duan, C.; Ren, X.; Lu, C. *Chem.—Eur. J.* **2011**, *17*, 9936–9943. (e) Lin, J.-D.; Long, X.-F.; Lin, P.; Du, S.-W. *Cryst. Growth Des.* **2010**, *10*, 146–157. (f) Xu, G.; Li, Y.; Zhou, W.-W.; Wang, G.-J.; Long, X.-F.; Cai, L.-Z.; Wang, M.-S.; Guo, G.-C.; Huang, J.-S.; Bator, G.; Jakubas, R. *J. Mater. Chem.* **2009**, *19*, 2179–2183. (g) Hang, T.; Fu, D.-W.; Ye, Q.; Xiong, R.-G. *Cryst. Growth Des.* **2009**, *9*, 2026–2029. (h) Fu, D.-W.; Zhang, W.;

- Xiong, R.-G. *Dalton Trans.* **2008**, 3946–3948. (i) Fu, D.-W.; Zhang, W.; Xiong, R.-G. *Cryst. Growth Des.* **2008**, 8, 3461–3464.
(17) Horiuchi, S.; Tokura, Y. *Nat. Mater.* **2008**, 7, 357–366.
(18) *Crystalclear, version 1.36*; Molecular Structure Corp. and Rigaku Corp.: The Woodlands, TX, and Tokyo, Japan, 2000.
(19) Sheldrick, G. M. *SHELXL-97 Program for X-ray Crystal Structure Refinement*; University of Göttingen: Göttingen, Germany, 1997.
(20) Spek, A. L. *PLATON-97*; University of Utrecht: Utrecht, The Netherlands, 1997.
(21) (a) Zhu, Q.-Y.; Wang, J.-P.; Qin, Y.-R.; Shi, Z.; Han, Q.-H.; Bian, G.-Q.; Dai, J. *Dalton Trans.* **2011**, 40, 1977–1983. (b) Wang, R. H.; Yuan, D. Q.; Jiang, F. L.; Han, L.; Gao, S.; Hong, M. C. *Eur. J. Inorg. Chem.* **2006**, 1649–1656. (c) Fernandez, G.; Corbella, M.; Mahia, J.; Maestro, M. A. *Eur. J. Inorg. Chem.* **2002**, 2502–2510. (d) Albelo, B.; Corbella, M.; Ribas, J.; Castro, I.; Sletten, J.; Stoeckli-Evans, H. *Inorg. Chem.* **1998**, 37, 788–798.
(22) (a) Liu, Y.; Zhang, H.; Tian, C.; Lin, P.; Du, S. *CrystEngComm* **2013**, 15, 5201–5204. (b) Zhang, Z.; Wojtas, L.; Zaworotko, M. J. *Cryst. Growth Des.* **2011**, 11, 1441–1445. (c) Ye, B. H.; Tong, M. L.; Chen, X. M. *Coord. Chem. Rev.* **2005**, 249, 545–565.
(23) Fisher, M. E. *Am. J. Phys.* **1964**, 32, 343–346.
(24) Goodenough, J. B. *Magnetism and Chemical Bond*; Wiley: New York, 1963.
(25) Zhao, J.-P.; Hu, B.-W.; Yang, Q.; Zhang, X.-F.; Hu, T.-L.; Bu, X.-H. *Dalton Trans.* **2010**, 39, 56–58.
(26) Wang, Z. M.; Zhang, B.; Fujiwara, H.; Kobayashi, H.; Kurmoo, M. *Chem. Commun.* **2004**, 416–417.
(27) (a) Berg, N.; Rajeshkumar, T.; Taylor, S. M.; Brechin, E. K.; Rajaraman, G.; Jones, L. F. *Chem.—Eur. J.* **2012**, 18, 5906–5918. (b) Ruiz-García, R.; Pardo, E.; Munoz, M. C.; Cano, J. *Inorg. Chim. Acta* **2007**, 360, 221–232. (c) Glerup, J.; Goodson, P. A.; Hodgson, D. J.; Michelsen, K. *Inorg. Chem.* **1995**, 34, 6255–6264.
(28) Rodriguez-Fortea, A.; Alemany, P.; Alvarez, S.; Ruiz, E. *Chem.—Eur. J.* **2001**, 7, 627–637.
(29) Scott, J. F. *J. Phys.: Condens. Matter* **2008**, 20, 021001.